CrossMark

Uniform Contribution of Supernova Explosions to the Chemical Enrichment of Abell 3112 out to R_{200}

Cemile Ezer[1,2], Esra Bulbul[3], E. Nihal Ercan[1], Randall K. Smith[2], Mark W. Bautz[3],
Mike Loewenstein[4,5], Mike McDonald[3], and Eric D. Miller[3]

[1] Department of Physics, Boğaziçi University, Istanbul, Turkey; cemile.ezer@boun.edu.tr
[2] Harvard-Smithsonian Center for Astrophysics, 60 Garden Street, Cambridge, MA 02138, USA
[3] Kavli Institute for Astrophysics & Space Research, Massachusetts Institute of Technology, 77 Massachusetts Avenue, Cambridge, MA 02139, USA
[4] NASA Goddard Space Flight Center, Greenbelt, MD, USA
[5] CRESST and X-ray Astrophysics Laboratory, NASA Goddard Space Flight Center, Greenbelt, MD 20771, USA

Abstract

The spatial distribution of the metals residing in the intra-cluster medium (ICM) of galaxy clusters records all the information on a cluster's nucleosynthesis and chemical enrichment history. We present measurements from a total of 1.2 Ms *Suzaku* XIS and 72 ks *Chandra* observations of the cool-core galaxy cluster Abell 3112 out to its virial radius (∼1470 kpc). We find that the ratio of the observed supernova type Ia explosions to the total supernova explosions has a uniform distribution at a level of 12%–16% out to the cluster's virial radius. The observed fraction of type Ia supernova explosions is in agreement with the corresponding fraction found in our Galaxy and the chemical enrichment of our Galaxy. The non-varying supernova enrichment suggests that the ICM in cluster outskirts was enriched by metals at an early stage before the cluster itself was formed during a period of intense star formation activity. Additionally, we find that the 2D delayed detonation model CDDT produce significantly worse fits to the X-ray spectra compared to simple 1D W7 models. This is due to the relative overestimate of Si, and the underestimate of Mg in these models with respect to the measured abundances.

Key words: galaxies: clusters: individual (A3112) – galaxies: clusters: intracluster medium – nuclear reactions, nucleosynthesis, abundances

1. Introduction

Clusters of galaxies are the largest concentrations of confined matter in the Universe. Their deep potential well retains all metals produced by stars and galaxies within the intra-cluster medium (ICM). Improved measurements of the ICM metallicity from X-ray observations provide direct information for the chemical enrichment history of the cluster, which mainly originates from supernova explosions (SNe) in the stellar populations. Understanding the evolution of the observed cluster enrichment is of vital importance, since these structures are unique probes of the nucleosynthesis and chemical enrichment of the Universe.

X-ray spectra of the ICM contain emission lines of heavy elements, which can only be produced by the late evolutionary stage of stars. From the observational results, the enriched abundance in the ICM is found to be larger than the total metal abundances found in the stellar population within the cluster (Portinari et al. 2004; Loewenstein 2006). This implies that the gas is not purely in the primordial state, but a considerable amount of it has been reprocessed within the galaxies and injected into the ICM. *ASCA* observations provided the first measurements of spatial distributions of heavy element abundances (e.g., iron [Fe] and silicon [Si]) in clusters of galaxies (Baumgartner et al. 2005). This pioneering result triggered studies for testing supernova models based on measured supernova (SN) yields. Using the limited *ASCA* measurements of abundance ratios, several studies investigated the efficiency of type Ia (SN Ia) and core collapse supernova (SN cc) enrichment in the ICM (e.g., Ishimaru & Arimoto 1997; Mushotzky & Loewenstein 1997; Dupke & White 2000; Finoguenov et al. 2000). These earlier studies suggest an early homogeneous enrichment by SN cc shortly after the cluster

formation, with its products well-mixed throughout the ICM. The launch of satellites such as *XMM-Newton* and *Chandra*, with improved spatial and spectral resolutions, enabled more precise measurements of elemental abundances and allowed determination of supernovae contribution to the metal enrichment in galaxy clusters' cores out to R_{500}[6] (Buote et al. 2003; Werner et al. 2006; Baldi et al. 2007; de Plaa et al. 2007; Matsushita et al. 2007). The subsequently discovered centrally peaked Fe abundance at the center of cool-core clusters may be explained by a more extensive period of enrichment by SN Ia explosions in the brightest cluster galaxy (Böhringer et al. 2004; De Grandi et al. 2004). This Fe enhancement in cluster cores is also seen in high spatial resolution observations with *XMM-Newton* (Simionescu et al. 2009; Bulbul et al. 2012b; De Grandi et al. 2014).

Studies of azimuthal spatial distributions of metal abundances out to cluster outskirts have become possible with the launch of *Suzaku*. Due to its low particle background, deep observations of clusters of galaxies with *Suzaku* provide the measurements of elemental abundances and SN ratio out to R_{200} in nearby clusters ($z < 0.02$), for example, the Perseus and Virgo clusters (Werner et al. 2013; Simionescu et al. 2015). These results suggest a uniform distribution of SN Ia and SN cc yields in the cluster outskirts, thus favoring an early enrichment by SN Ia started in the early stages of the cluster formation.

Extending these studies to more distant clusters has become possible through deep *Suzaku* observing programs. Abell 3112 (hereafter Abell 3112) is one such object, an archetypal cool-

---

[6] R_{500} is the radius at which the mean density of the cluster is 500 times the critical density of the Universe at the cluster's redshift.

core cluster at redshift 0.075. The cluster has a strong radio source, PKS 0316–44, located in the cluster center (Takizawa et al. 2003). The mass deposition rate of $10^{+7}_{-5}\,M_\odot\,yr^{-1}$ indicated by *XMM-Newton* observations is much less than the expected rate from cooling flow clusters (O'Dea et al. 2008; Bulbul et al. 2012a). It was also reported that a soft X-ray gas was present in the ICM above the contribution from the diffuse 4–5 keV hot gas. This soft excess was first thought to be well described with an additional non-thermal power-law model or with a 1 keV thermal model of low metal abundance (Nevalainen et al. 2003; Bonamente et al. 2007; Lehto et al. 2010). However, Bulbul et al. (2012a) ruled out the thermal origin of this soft excess using *XMM-Newton RGS* observations, leaving the possibility for non-thermal interpretation of a potential population of relativistic electrons with ∼7% of the cluster's gas pressure. The peaked Fe, Si, and S abundances in the core region reported in Bulbul et al. (2012a, 2012b) imply an ongoing SN Ia contribution toward the immediate cluster core (<0.′5), followed by a more uniform SN cc contribution. Finally, Bulbul et al. (2012b) used higher resolution *XMM-Newton RGS* observations of Abell 3112 to constrain the SNe models using a new method, *snapec*, and reported that 30.3% ± 5.4% of the total SN which enriched the ICM are SN Ia within the immediate core (∼50 kpc) of the cluster. It was also reported that the total number of SN explosions required to create the observed metals is $(1.06 \pm 0.34) \times 10^9$ in the cluster core (Bulbul et al. 2012b).

In this paper, we take a step further to investigate the radial distribution of SN enrichment in Abell 3112 out to the cluster's virial radius by comparing deep *Suzaku* and *Chandra* X-ray observations with the nucleosynthesis models available in the literature. The paper is organized as follows: we describe *Suzaku* and *Chandra* data analysis in Section 2. In Section 3, we give an overview of spectral extraction and background modeling. The systematic uncertainties relevant to *Suzaku* analysis are described in Section 4. We provide our results and conclusions in Sections 5 and 6.

At the cluster's redshift, 1′ corresponds to ∼82 kpc. The cosmological parameters used in the analysis are $H_0 = 73$ km s^{-1} Mpc^{-1}, $\Omega_M = 0.27$, $\Omega_\Lambda = 0.73$. Unless otherwise stated, reported errors correspond to 68% confidence intervals.

2. Observations and Data Reduction

2.1. Suzaku Data Reduction

Abell 3112 was observed with *Suzaku* with five pointings between 2008 May and 2014 December. The unfiltered *Suzaku* data are analyzed by using HEASOFT version 6.17 and the latest calibration database (CALDB) as of 2015 November. Here we summarize the data analysis steps briefly. The details of *Suzaku* data reduction are described in Bulbul et al. (2016a, 2016b). The FTOOL *aepipeline* is used to reprocess the unfiltered event data files using the latest calibration and screening criteria. Additionally, we require elevation angles above 5° and 20° for the night and day Earth rim and the geomagnetic cutoff rigidity of >6 GV. The data taken when the satellite passes through the regions affected by the South Atlantic Anomaly (SAA) and the ^{55}Fe calibration sources at two far corners of CCD chips are excluded from the analysis. The event files in the 3×3 and 5×5 editing modes are combined. An additional correction for the comparable fraction of flickering pixels is applied to the data

taken after 2014 January.[7] The filtered exposure times are given in Table 1. A total of 1.2 Ms total filtered *Suzaku* XIS exposure time (391 ks exposure per XIS detector) is used in this analysis. The non-X-ray background (NXB) images are generated using the "night-Earth" data (NTE) via the FTOOL *xisnxbgen* (Tawa et al. 2008). The NXB images are then subtracted from the mosaicked image prior to exposure correction. We generate the exposure maps as described in Bautz et al. (2009) and Bulbul et al. (2016a, 2016b) using *xissim* and *xisexpmapgen*. Before exposure correction is applied, underexposed regions with <15% of the maximum exposure time are removed. An exposure corrected and particle background subtracted *Suzaku* mosaic image is shown in the left panel of Figure 1.

2.2. Chandra Data Reduction

To detect X-ray point sources unresolved by *Suzaku*, we use the two overlapping *Chandra* pointings of the cluster. *Chandra* ACIS-I data are filtered from background flares using LC_CLEAN through *Chandra* analysis software CIAO version 4.7 with CALDB version 4.6.7. The filtered light curves show no leftover significant background flares. The filtered exposure times are given in Table 1. We extract an image in the 0.5–7 keV band. The background image is extracted from the blank-sky observations. To account for variations in the particle background, we use count rates detected in the 9–12 keV band to match Abell 3112 observations, as described in Markevitch et al. (2003). The CIAO's *wavdetect* tool is used to determine the locations of the point sources in the field of view (FOV). The point sources detected by *Chandra* in the *Suzaku* FOV are shown in the right panel of Figure 1.

3. Spectral Modeling and Background Subtraction

Eliminating the contribution from local foreground, extra-galactic background, and the point sources within the *Suzaku* FOV is crucial in studies of cluster outskirts. In this section, we first describe our spectral fitting procedure for cluster emission. Additionally, we describe our background subtraction and point source optimizations methods in Sections 3.2 and 3.3.

3.1. Cluster Emission Modeling

To examine the spectral properties of Abell 3112, we extract spectra in five regions surrounding the cluster's centroid from the filtered event files in *XSELECT* for each XIS sensor (see Figure 1). The selected regions cover a radial range from the cluster core out to the virial radius (R_{200}; Region 1, 0′–2′; Region 2, 2′–4′; Region 3, 4′–6′; Region 4, 6′–8′; and Region 5, 8′–18′). The regions are selected based on the total source counts ($>10^4$ counts) in each. The overdensity radii R_{500} and R_{200} are also marked in Figure 1. The FTOOLS *xissimarfgen* and *xisrmfgen* are used to generate the effective area ancillary response file (ARF) and detector redistribution matrix file (RMF), respectively. For each annulus and each observation, we merge data from front-illuminated (FI) XIS0 and XIS3 detectors. The back-illuminated (BI) XIS1 data are fit simultaneously with the FI spectra. Spectral fitting is performed in the 0.7–7 keV energy band where the *Suzaku* XIS detectors are the most sensitive. The cluster emission is modeled with ATOMDB version 2.0.2 (Smith et al. 2001; Foster et al. 2012).

---

7 http://www.astro.isas.jaxa.jp/suzaku/analysis/xis/nxb_new/

Table 1
Suzaku and *Chandra* observations of Abell 3112

Instrument	Obs. ID	Pointing	R.A. (J2000)	Decl. (J2000)	Observation Date	Exp. XIS0/XIS1/XIS3 (ks)	Filtered Exp. XIS0/XIS1/XIS3 (ks)	PI
Suzaku XIS	803054010	On-axis	49.478	−44.248	2008 May 23	67.5/67.5/67.5	54.9/54.9/54.9	M. Bonamente
	808068010	On-axis	49.498	−44.251	2013 Jun 23	119.1/119.1/119.1	113.5/113.5/113.5	E. Bulbul
	808068020	On-axis	49.497	−44.236	2013 Jun 25	65.4/65.4/65.4	54.4/54.4/54.4	E. Bulbul
	809116010	Offset	49.354	−44.489	2014 Dec 09	107.9/107.9/107.9	87.3/87.3/87.3	E. Bulbul
	809116020	Offset	49.354	−44.449	2014 Dec 12	97.9/97.9/97.9	80.4/80.4/80.4	E. Bulbul
Chandra ACIS-I	13135	On-axis	49.481	−44.258	2011 Mar 14	42.8	42.2	S. Murray
	6972	Offset	49.421	−44.410	2006 Apr 18	30.2	29.7	M. Markevitch

XSPEC v12.9.0 is used to perform the spectral fits with the extended C-statistic as an estimator of the goodness of the fit (Arnaud 1996).

The soft local foreground and cosmic X-ray background parameters are fixed to the best-fit values obtained from the joint fit of the *ROSAT* All Sky Survey (*RASS*) and local background, as described in Section 3.3. The particle background spectra are subtracted prior to fitting. The spectra are fit with a single-temperature thermal model (1T *apec* or *snapec*) with free temperature, metallicity, and normalization. We also search for two-temperature structure by adding a second thermal component (2T *apec*). The Galactic Column density is fixed to the LAB value of 1.33×10^{20} cm^{-2} in our fits (Kalberla et al. 2005) and solar abundances adopted from Anders & Grevesse (1989). The redshift is fixed to 0.075 (Braglia et al. 2011).

Cutoff-rigidity-weighted non-X-ray background (NXB) spectra are extracted from the night-time-earth data for each detector using the *xisnxbgen* tool. NXB event files are reprocessed following the same procedure described in Section 2. The same annular sections are used to produce NXB spectra in *XSELECT* after the calibration sources are removed.

3.2. Point Sources Optimization

The main obstacle in excising point sources in analyses of *Suzaku* observations is the relatively large size of point-spread-function (PSF) of the *Suzaku* mirrors. We use the two overlapping *Chandra* observations (both on-axis and offset) to detect X-ray point sources unresolved by *Suzaku* (see Section 2.2). The PSF sizes of *Suzaku* and *Chandra* are quite different. Therefore the extents of the point sources detected by *wavdetect* using *Chandra* observations cannot be used directly to exclude point sources in the *Suzaku* FOV. We use the same procedure described in detail in Bulbul et al. (2016b) to determine a conservative exclusion radii for point sources detected by *Chandra* pointings. We selected the brightest point source in the *Suzaku* FOV (J2000; R.A.: $49°342$; Decl.: $−44°173$), which is located in a fairly faint region of the cluster (shown in the green circle in Figure 1). The *Chandra* spectrum of the point source is extracted using the *specextract* tool in *CIAO*. The spectrum of the source is fitted with an absorbed power-law with a fixed index set to 1.4 and variable normalization (Hickox & Markevitch 2006). We then simulate *Suzaku* observations of the point source based on the best-fit flux (3.47×10^{-5} photons keV^{-1} cm^{-2} s^{-1}) and on the power-law index (1.4) obtained from the *Chandra* observations using

the FTOOL *xissim*. To estimate the effect of the point source contamination on the surrounding cluster ICM gas, we add simulated diffuse emission to the spectrum, with a total net count of 2000. Our goal is to measure the plasma temperature with better than <20% accuracy in these simulations. We extract the spectrum around the point source with incremental extraction radii to determine the radius where the cluster emission is not affected by the point source contamination. We find that excluding $r > 40''$ around the point source has a minimal effect on the cluster plasma temperature, metallicity, and normalization. Since this point source is in a faint region of the cluster and all our spectra include at least 10^4 counts, the exclusion radius of $40''$ is a conservative estimate for all point sources detected by *Chandra* observations in the *Suzaku* FOV. The exclusion radius is shown in the lower left corner of Figure 1 (left panel).

3.3. Modeling of the Local X-Ray Background

Understanding temporal and spatial variations in the local X-ray background is crucial in analyses of faint cluster outskirts. The variable soft X-ray background must be examined carefully before the spectral fits are performed. We first extract a local background spectrum from the outermost region (Region 6 in Figure 1, $18'$–$24'$, which is beyond R_{200}), where the expected contribution from the cluster thermal emission is minimal. We also extract the *RASS* data from a 1–2 degree annulus surrounding the central sub-cluster's centroid.[8] The *RASS* background spectrum is simultaneously fit with the local background XIS FI and BI spectra. The local X-ray background model consists of two absorbed thermal components (*apec*) for the Galactic Halo (GH; E ∼ 0.25 keV) and the Hot Foreground (HF; E ∼ 0.75 keV), an unabsorbed thermal model for the Local Hot Bubble (LHB; E ∼ 0.1 keV), and a power-law component for unresolved point sources (cosmic X-ray background; CXB), with a photon index of 1.4 (Hickox & Markevitch 2006). We note that we use the full energy band between 0.5 and 7 keV bands for XIS spectra and 0.5–2 keV for RASS spectra in background fits in order to have a better handle on the soft GH component. In order to avoid degeneracies between the three thermal background components, we fix the temperatures to the values reported in Snowden et al. (2008) and Bulbul et al. (2012a). We also add two Gaussian models to eliminate the O VII and O VIII lines from solar wind charge exchange at 0.56 keV and 0.65 keV. The metallicities of these *apec* models are set to solar, while the
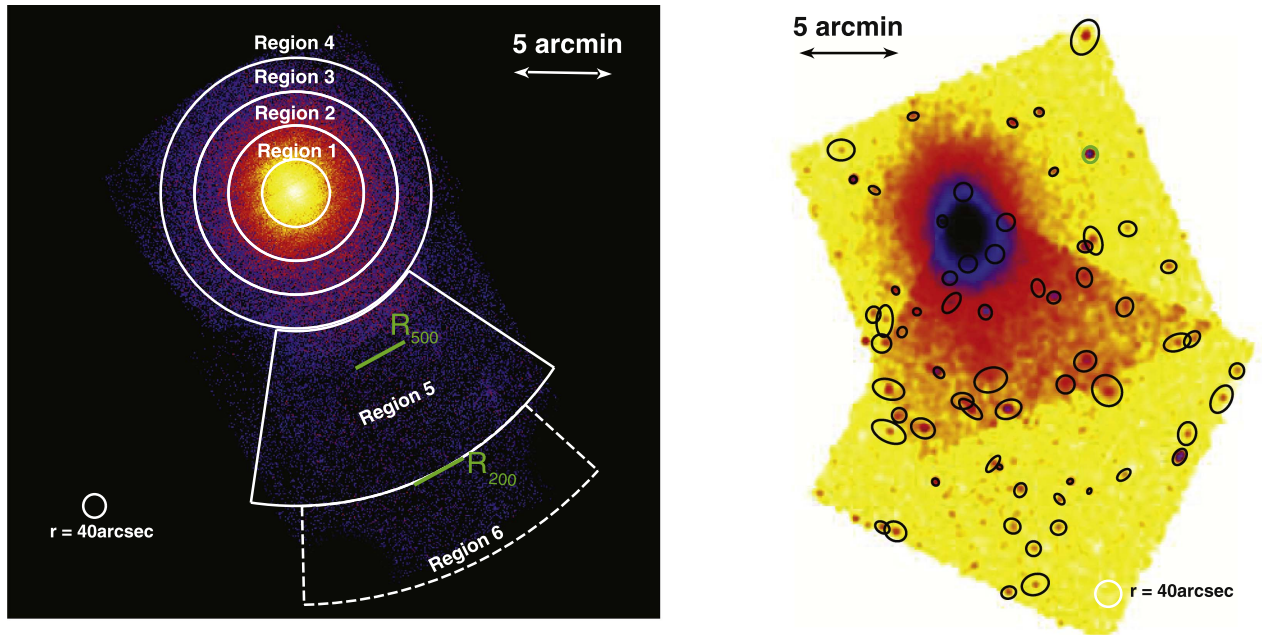
---

8 http://heasarc.gsfc.nasa.gov/cgi-bin/Tools/xraybg/xraybg.pl

Figure 1. Left panel: exposure corrected, NXB background subtracted *Suzaku* XIS image of Abell 3112. The image is extracted in the 0.5–7 keV energy range. The spectral extraction regions out to R_{200} are shown in white. The region that is used to extract the local background spectrum is shown in dashed lines. The overdensity radii R_{500} and R_{200} are marked with green bars in the figure. The point source exclusion radius of $40''$ is shown in the lower corner of the image. Right panel: background subtracted *Chandra* image of Abell 3112 is given in 0.5–7.0 keV energy band. *Chandra* pointings are used to detect point sources within the *Suzaku* FOV. The brightest point source, which is used in estimating point-source exclusion extent, is shown in the green.

redshifts are fixed at zero. We find a good fit with $C-$stat value of 507.3 for 341 dof. The best-fit values of the background model are given in Table 2. The best-fit normalization of the power-law is $1.41^{+0.14}_{-0.14} \times 10^{-7}$ photons keV^{-1} cm^{-2} s^{-1} arcmin^{-2} at 1 keV, corresponding to a CXB flux of $4.3 +/- 0.4 \times 10^{-12}$ erg s^{-1} cm^{-2} deg^{-2} in the 0.5–2 keV band.

4. Systematic Uncertainties

The analyses of low-surface brightness regions of clusters with *Suzaku* may be subject to systematic uncertainties. To estimate the magnitude of these, we consider the following potential sources of uncertainties: (i) systematics associated with the CXB level; (ii) systematics due to variations in the soft X-ray and particle background; (iii) contamination due to stray light and the large size of the PSF of *Suzaku*'s mirrors. We describe how we estimate and handle these in detail in the following sections.

4.1. The Cosmic X-Ray Background

The variations in the unresolved CXB within the XIS FOV can be a source of serious systematic uncertainty. Following the same approach in Bulbul et al. (2016b), we find that the detection limit in our observations is 6.7×10^{-14} erg cm^{-2} s^{-1} in the 2.0–10.0 keV energy band. The contribution of unresolved point sources to the total flux is calculated using the formula given in Moretti et al. (2003):

$$F_{\text{CXB}} = 2.18 \pm 0.13 \times 10^{-11} - \int_{S_{\text{excl}}}^{S_{\text{max}}} \left(\frac{dN}{dS} \right)$$
$$\times S \, dS \text{ erg cm}^2 \text{ s}^{-1} \text{ deg}^{-2}, \qquad (1)$$

where the cumulative number of point sources per flux indicated as dN/dS is integrated over the detection limit from

Table 2
Best-fit Parameters from Fits to Soft X-ray Background

Component	kT (keV)	Normalization 10^{-8} cm^{-5}	Flux (0.5–2.0 keV) 10^{-16} erg s^{-1} cm^{-2}
GH	0.25[a]	$0.80^{+0.70}_{-0.60}$	$0.14^{+0.09}_{-0.09}$
HF	0.75[a]	$1.20^{+0.30}_{-0.30}$	$0.34^{+0.07}_{-0.07}$
LHB	0.10[a]	$68.4^{+6.20}_{-6.40}$	$1.29^{+0.12}_{-0.11}$

Note.
[a] Indicates fixed parameters in the background fits. The temperatures are fixed to value reported in Snowden et al. (2008).

the lower bound $S_{\text{excl}} = 6.7 \times 10^{-14}$ erg cm^{-2} s^{-1} to the upper bound $S_{\text{max}} = 8.0 \times 10^{-12}$ erg cm^{-2} s^{-1}, given in Moretti et al. (2003). We use a total flux of $2.18 \pm 0.13 \times 10^{-11}$ erg cm^{-2} s^{-1} deg^{-2} obtained from *Swift* data (Moretti et al. 2009). This flux is also consistent with the total CXB flux from *Chandra* and *XMM-Newton* observations (Moretti et al. 2003; De Luca & Molendi 2004). For the populations of the point sources, we adopt an analytical model provided in Moretti et al. (2003):

$$N(>S) = N_0 \left[\frac{(2 \times 10^{-15})^\alpha}{S^\alpha + S_0^{\alpha - \beta} S^\beta} \right], \qquad (2)$$

where the best-fit parameters are $N_0 = 5300^{+2850}_{-1400}$, $S_0 = (4.5^{+3.7}_{-1.7}) \times 10^{-15}$ erg cm^{-2} s^{-1}, $\alpha = 1.57^{+0.10}_{-0.08}$, and $\beta = 0.44^{+0.12}_{-0.13}$. Using the best-fit parameters of hard energy band given in Moretti et al. (2003), we find that the unresolved flux contribution in the 2–10 keV band to the CXB flux is $1.38 \pm 0.62 \times 10^{-11}$ erg cm^{-2} s^{-1} deg^{-2}.

Table 3
Estimated 1σ Fluctuations in the CXB Level Due to Unresolved Point Sources in the *Suzaku* FOV in Units of 10^{-12} erg cm^{-2} s^{-1} deg^{-2}

	Region 1	Region 2	Region 3	Region 4	Region 5
CXB Fluc.	10.10	5.78	4.48	3.78	2.12

The deviations from the expected CXB level due to the unresolved point sources are

$$\sigma_B^2 = \frac{1}{\Omega} \int_0^{S_{\mathrm{excl}}} \left(\frac{dN}{dS}\right) \times S^2 \, dS, \qquad (3)$$

where Ω is the solid angle. We then calculate 1σ rms CXB fluctuations using Equations (1) and (2) for each region. The results are shown in Table 3. We find that a typical 1σ uncertainty on the measured CXB level is comparable to the rms value of CXB fluctuations. We note that this uncertainty is used in Section 4.2 to account for the CXB variations. These systematics are included in the final systematic errors on the observable quantities.

4.2. Systematics due to Variations in the Soft X-Ray and Particle Background

We model the soft X-ray background by jointly fitting the *ROSAT* data with the local X-ray background spectra (including LHB, GH, HF), and CXB obtained from the annuli encompassing the $18'$–$24'$ region. To take into account the spatial variations that may dominate the background, we perform 1000 Markov chain Monte Carlo (MCMC) realizations of the best-fit background model. The model parameters are allowed to vary within their 1σ uncertainty range. An uncertainty up to 3.6% on the NXB level is also taken into account in these realizations (Tawa et al. 2008). We find that the systematic variations in the soft foreground, CXB, and the particle background level have an effect of $<1\%$ on the best-fit temperatures and normalizations of Regions 1 and 2. Variations up to 2%, 6%, and 16% are measured in Regions 3, 4, and 5. The uncertainties due to the variation in the soft X-ray background are taken into account in the total error budget calculations by adding them in quadrature.

4.3. Systematics due to Scattered Light and PSF Scattering

The relatively large size of the *Suzaku* mirror PSF ($\sim 2'$) may cause photons emitted from a particular region in the sky to be detected elsewhere on the detector. We note that the size of each spectral extraction region used in this work is larger than the PSF size, minimizing the effect of PSF scattering in this analysis. To estimate the magnitude of this uncertainty, we use the ray-tracing simulator *xissim* to generate *Suzaku* event files using Ishisaki et al. (2007). The *Chandra* ACIS images and the best-fit *Suzaku* spectral models are used to simulate event files of each XIS sensor with 1×10^6 photons. The image of each sector shown in Figure 1 (left panel) is extracted from the simulated event files. The percentile contribution of the flux on each sector from adjacent regions are shown in Table 4. Columns refer to the percentage fluxes providing the flux, while the rows refer to the percentage fluxes receiving the flux in Table 4. For instance, 3.47% (first row, third column) is the fraction of photons leaked from Region 1 contaminating

Table 4
Percentage Contribution of PSF Scattering

	Region 1	Region 2	Region 3	Region 4	Region 5
Region 1	68.5	15.6	3.47	1.33	0.33
Region 2	14.3	65.6	16.4	2.25	0.38
Region 3	0.24	17.7	64.5	13.7	0.82
Region 4	0.26	1.52	15.2	66.8	6.81
Region 5	0.09	0.27	0.79	7.06	89.2

Region 3. As clearly seen in Table 4, most of the photons that originate from one particular annulus in the sky are detected in the same region on the detector, while up to 17% of the photons may be detected in the surrounding annuli. However, the fraction of photons detected in the outermost annulus that scatter from the inner regions is negligibly small ($<1\%$). The results are consistent with the fractions reported in Bautz et al. (2009) and Bulbul et al. (2016b).

To estimate the effect of the PSF scattering and the scattered light contribution to the variables (e.g., temperature and metallicity), we jointly fit the spectra of each sector with the normalizations scaled according to the reported fractions in Table 4. Although the uncertainty on the measured temperature is smaller than the statistical errors in each sector, we added these in quadrature to the total error budget of the thermal model variables.

5. Results

We start with examining the global properties of the cluster by modeling the five spectra using the thermal models as described in Section 3. The results for the chemical enrichment are also described in this section.

5.1. Global Spectral Properties

To examine the global temperature and metallicity out to R_{200} of Abell 3112, we first fit the spectra with a 1T *apec* model. The model parameters between different observations are tied to each other. The best-fit projected temperature together with their systematic and statistical uncertainties are shown in Figure 2 and Table 5. In the same figure, the *Suzaku* results are compared with the previous measurements from the *XMM-Newton* observations (Bulbul et al. 2012a). The *Suzaku* and *XMM-Newton* results are in agreement with each other at 1σ confidence level from the cluster core out to R_{500}. The plasma temperature in the core (4.27 ± 0.01 keV) is cooler than the temperature at intermediate radii, confirming that Abell 3112 is a cool-core cluster. While previous observations were able to measure the temperature only out to R_{500}, we are able to measure the ICM temperature to R_{200}, owing to *Suzaku*'s lower particle background.

In order to investigate the multi-phase gas in the ICM, we fit the spectra with a 2T *apec* model. The best-fit model parameters are given in Table 6. The best-fit temperature of the ICM in Region 1 becomes 5.86 ± 0.37 keV, with a lower kT component of $3.23^{+0.07}_{-0.14}$ keV. The temperature in Region 2 is $5.63^{+0.60}_{-0.26}$, with a lower kT component of $3.41^{+0.42}_{-0.21}$ keV. The metallicity remains unchanged in both regions with an addition of the second *apec* model. Adding the second thermal component decreases ΔC-stat of the fit to the spectra of Region 1 and Region 2 (ΔC-stat = 126 for 2 dof in Region 1; ΔC-stat = 17 for 2 dof in Region 2). C-statistics do not
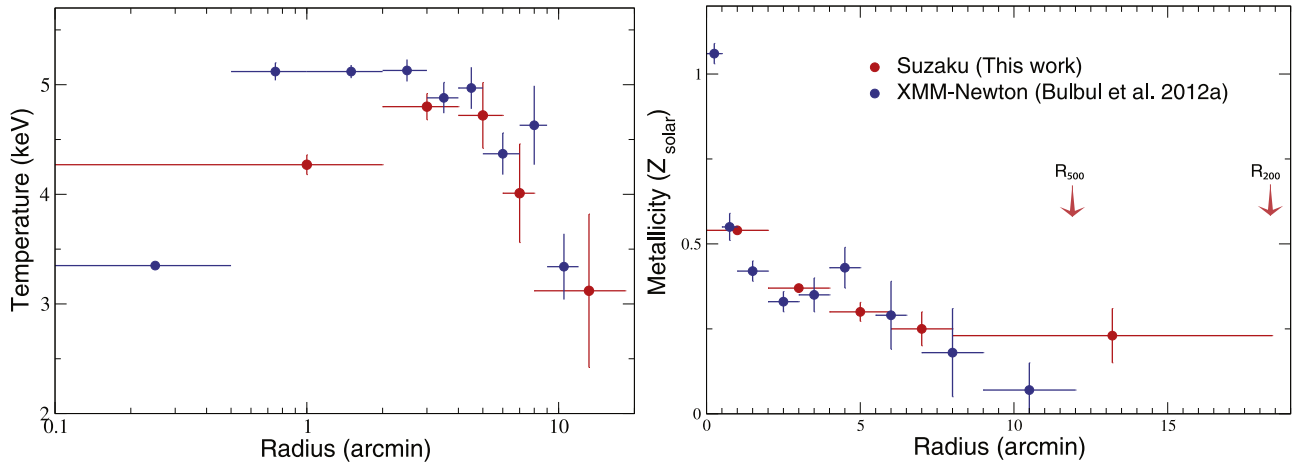
Figure 2. Radial profile of temperature (left panel) and metallicity (right panel) for Abell 3112 obtained from a single temperature *apec* model. The statistical errors (68% confidence level) together with systematics on the *Suzaku* results are overplotted. *Suzaku* results are compared with the *XMM-Newton* results reported by Bulbul et al. (2012a). The *XMM-Newton* and *Suzaku* measurements are in agreement with each other at 1σ level. While *XMM-Newton* observations are able to determine the temperature and metallicity from the core out to R_{500}, we are able to measure these parameters out to R_{200} of the cluster.

Table 5
Best-fit Parameters of the 1T *APEC* Model

Region	kT (keV)	Metallicity ($Z_\odot$)	N (10^{-6}cm^{-5})	C-stat (dof)
Region 1	4.27 ± 0.02	0.54 ± 0.01	881.0 ± 2.4	1260.9 (849)
Region 2	4.81 ± 0.04	0.36 ± 0.01	204.1 ± 2.9	1383.6 (1135)
Region 3	4.66 ± 0.05	0.26 ± 0.03	71.7 ± 0.14	997.3 (844)
Region 4	4.26 ± 0.10	0.25 ± 0.05	22.3 ± 2.3	397.9 (279)
Region 5	3.37 ± 0.77	0.22 ± 0.08	1.1 ± 0.2	264.9 (136)

Table 6
Best-fit Parameters of the 2T *APEC* Model

Parameter	Region 1	Region 2
kT_1 (keV)	$3.24^{+0.20}_{-0.16}$	$3.41^{+0.07}_{-0.09}$
N_1 (10^{-4} cm^{-5})	$4.32^{+0.90}_{-0.78}$	$0.65^{+0.08}_{-0.06}$
kT_2 (keV)	$5.94^{-0.16}_{-0.15}$	5.63 ± 0.10
N_2 (10^{-4} cm^{-5})	$4.46^{+0.78}_{-0.77}$	$1.41^{+0.15}_{-0.26}$
Metallicity ($Z_\odot$)	0.55 ± 0.01	0.37 ± 0.01
C-stat	1135.52 (847)	1366.25 (1133)

Figure 3. Radial distribution of elemental abundances of α-elements, Si, S, Mg, and Fe. We are able to determine Mg and Fe abundances out to R_{200}. The uncertainties are for $\Delta C = 1$.

provide a direct statistical test to quantify the significance of the improvement in adding the secondary *apec* component. We therefore calculate the corresponding χ^2 values from the best-fits (which are obtained using C-statistics). The improvement in χ^2 values are 114 and 12 in Region 1 and Region 2 for two extra dof (temperature and normalization of the second *apec* model). This corresponds to F-test values of 40.8 and 4.9, with null hypothesis probabilities of 10^{-25} and 0.7% in Regions 1 and 2. Comparing the normalizations of the 2T *apec* models, both components are equally contributing the total emission (see Table 6). The temperatures measured in the 0′–2′ region of *Suzaku* observations are consistent with the temperatures reported from *XMM-Newton* observations in the cluster core (Bulbul et al. 2012a). The limited statistics of the spectra extracted from Regions 3, 4, and 5 do not allow for the testing of the multi-phase nature of the plasma in these regions. We therefore do not provide the 2T results from those fits here.
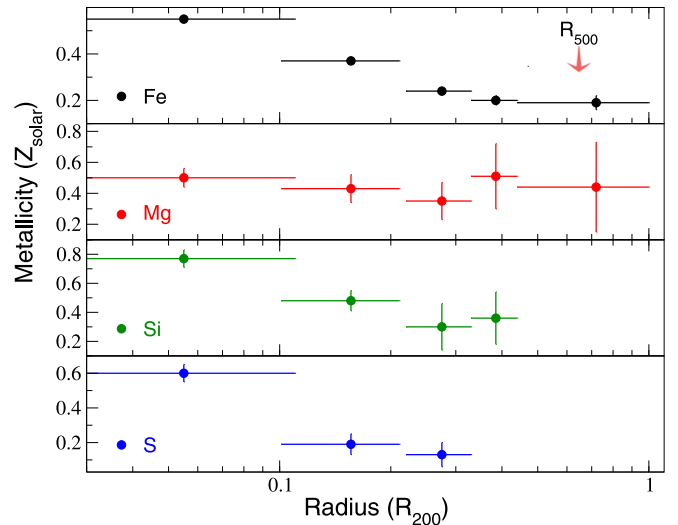
We also compare metallicity profiles obtained from *XMM-Newton* and *Suzaku* observations in Figure 2. While *XMM-Newton* observations can accurately constrain the profiles in the core of the cluster out to $\sim 0.5R_{500}$, *Suzaku* observations are able to constrain metallicity at radii out to R_{200}. The regions that are covered by both *XMM-Newton* and *Suzaku* observations are in agreement with each other at the 1σ level.

The metallicity profile is peaked at the center, and remains fairly constant beyond $\sim 0.5R_{500}$. The overall metallicity of the ICM (mostly driven by the Fe lines) in the cluster outskirts is $0.25 \pm 0.05\ Z_\odot$ and $0.22 \pm 0.08\ Z_\odot$ in Regions 4 and 5, which cover the region from $0.5R_{500}$ to R_{200}. These values are consistent with metallicities measured in the outskirts of low-mass clusters (Fujita et al. 2008; Bulbul et al. 2016b). We further investigate the radial abundance distributions of individual α-elements, such as Si, S, Fe, and magnesium (Mg) out to R_{200} (see Figure 3). The fits are performed with a single temperature *vapec* model. The Fe, Si, S, and Mg elemental abundances are allowed to vary independently, while

other elemental abundances that cannot be measured (e.g., carbon and argon) are fixed to the measured Fe abundance at the outskirts, 0.25 $Z_\odot$. We find that Si, S, and Fe abundances show an increasing trend toward the core of the cluster, confirming the results from *XMM-Newton* observations. We are also able to extend the detection of Si out to $\sim 0.5R_{200}$ in the *Suzaku* observations, while previous *XMM-Newton* observations report the detection of these metals only in the very central region ($< 0.06R_{200}$; see Bulbul et al. 2012a).

SN Ia produce large amounts of Fe, while lighter elements, such as Mg, are produced mainly by SN cc. Measurements of the radial profile of Mg and Fe abundances within the ICM provide clues regarding the relative contribution of different types of supernovae to the chemical enrichment. For instance, SN cc products are thought to be produced early on in the formation history of clusters at $z \sim 2$–3 (Simionescu et al. 2015). We therefore investigate distributions of these elements in the outskirts of Abell 3112. We perform fits to the observed Mg and Fe profiles with phenomenological models to quantify the change in their distribution with radius. In a power-law model fit to the observed Mg profile, the best-fit normalization is 0.35 ± 0.12 and an index of 0.11 ± 0.15. We find a good fit with overall χ^2 of 0.62 (3 dof). Although the power-law index in this fit indicates a slight decline with radius, it is consistent with zero. This indicates that the distribution of the Mg is consistent with a uniform profile. However, due to large uncertainties, neither the uniform profile nor the peaked profile can be excluded based on the *Suzaku* data.

We observe a steeper decline in the Fe abundance profile with a power-law index of 0.54 ± 0.15, and normalization of 0.13 ± 0.03. The overall χ^2 is 1.37 for 3 dof. The observed slope of the Fe profile is steeper compared to the Virgo cluster (Simionescu et al. 2015). The Fe abundance peaks in the core of Abell 3112 (similar to those of S and Si); however, it becomes uniform beyond $0.2R_{200}$ at a level of ~ 0.2–$0.24\ Z_\odot$. The uniform abundance in the outskirts of the cluster is consistent with the Fe abundance observed in the *Suzaku* observations of the nearby clusters (e.g., the Perseus cluster; Werner et al. 2013). Additionally, the mean observed value at the outskirts of Abell 3112 is consistent with both the Perseus and Virgo clusters.

5.2. Radial Distribution of SN Ia to SN cc Fraction

A commonly used method to constrain the distribution of SN enrichment in clusters of galaxies is to examine the relative abundances of metals that are produced by SN Ia and SN cc (de Plaa et al. 2007). Detailed studies of high signal-to-noise *Suzaku* data of the nearby Perseus cluster ($z = 0.018$) and Virgo cluster ($z = 0.004$) have provided tight constraints on the fractional distribution of SN enrichment out to R_{200} using S, Si, and Mg abundance ratios with respect to Fe (Werner et al. 2013; Simionescu et al. 2015). However, it is challenging to perform this method for higher redshift clusters such as Abell 3112, since the detection of abundances of key elements (e.g., Si and S) extends only out to an intermediate radius ($\sim 0.5R_{200}$). Additionally, the uncertainty of the observed Mg abundance is large in our observations. Therefore we use an alternative approach here to measure the SN fraction out to the virial radius.

To investigate the percentage contribution of SN explosions that enrich the ICM, we fit the spectra with the *snapec* model

Table 7
Best-fit Parameters of the *snapec* Model to the *Suzaku* Spectrum of Region 1

SN Ia Model	N_{SNe} ($\times 10^9$)	R	C-stat (dof)
W7	3.61 ± 0.16	0.10 ± 0.01	1112.4 (840)
W70	3.59 ± 0.25	0.10 ± 0.02	1108.9 (840)
WDD	3.24 ± 0.10	0.12 ± 0.02	1108.1 (840)
CDD	3.18 ± 0.15	0.12 ± 0.01	1108.8 (840)
CDDT	3.08 ± 0.28	0.41 ± 0.09	1173.3 (840)
ODDT	3.06 ± 0.21	0.18 ± 0.03	1112.3 (840)

implemented in the *XSPEC* fitting package (Bulbul et al. 2012b).[9] The *snapec* model compares the SN yields available in the literature to X-ray spectra in a given energy band. The model has five free parameters: the total integrated number of SNe (N_{SNe}) per $10^{12}\ M_\odot$ of ICM plasma (i.e., rescaled to yield values appropriate for cluster cores since the cluster's formation), the ratio of SN Ia to SN cc (R), plasma temperature (kT), redshift, and normalization. After the fit is performed, the goodness of the fit can be used as a test for SN yields. The advantage of this model is that it uses all available elements to constrain the fractional contribution of SNe to chemical enrichment of the ICM, as opposed to determining SN enrichment from individual elemental abundance ratios. The *snapec* model provides a self-consistent set of physical parameters, SN fraction, and the total number of SNe. Therefore statistical uncertainties on these parameters are greatly reduced because of the larger number of elemental abundance measurements used in deriving the constraints. Additionally, the method allows the user to choose between different SN enrichment models, and the goodness of the overall fit can be used to test SN enrichment models when finer resolution X-ray observations are available (see Bulbul et al. 2012b for *Hitomi* simulations). This method is specifically helpful for the case here, where we have low signal-to-noise data.

We use a variety of SN yields from the literature in this work. Among the SN Ia yields are one-dimensional spherically symmetric slow deflagration models W7 and W70; delayed detonation models referring to WDD and CDD from Iwamoto et al. (1999, hereafter I99) and Nomoto et al. (2006, hereafter N06); and two-dimensional delayed detonation models, including symmetric (CDDT) and asymmetric (ODDT) explosions from (Maeda et al. 2010, hereafter M10). Meanwhile, for the SN cc yields, we use the Iwamoto et al. (1999) Salpeter-IMF-average yields calculated for a large range of progenitor masses (10–50 $M_\odot$) and metallicities (0–1 $Z_\odot$). We first fit the spectrum extracted from Region 1 using a set of yields from various SN enrichment models. The goodness of the fits of various SN Ia yields are shown in Table 7. We find that the I99 WDD model describes the *Suzaku* data of the immediate core region the best, with a C-stat of 1108.13 (840 dof), where we have the highest signal-to-noise data. The I99 W7, CDD, and WDD SN Ia models produce equally good fits to the data with ΔC-stat of 3–4 for the same number of dof. Indeed, W7, WDD, and CDD models predict similar amounts of Fe and Mg. Since the most significantly detected lines in our spectra are Fe-L and Fe-K shell lines, they are likely to be responsible for the similarly observed C-stat values in our fits

---

[9] http://heasarc.gsfc.nasa.gov/xanadu/xspec/models/snapec.html

Table 8
Best-fit Parameters of the *snapec* Model Obtained Using I99 WDD SN Ia and
I99 SN cc Yields

	N_{SNe} ($\times 10^9$)	R	C-stat (dof)
Region 1	3.24 ± 0.10	0.12 ± 0.02	1108.1 (840)
Region 2	1.96 ± 0.36	0.16 ± 0.02	1079.9 (842)
Region 3	1.48 ± 0.13	0.12 ± 0.04	1008.9 (850)
Region 4	1.22 ± 0.12	0.13 ± 0.05	337.3 (259)
Region 5	0.87 ± 0.17	0.11 ± 0.06	244.2 (151)

Figure 4. Radial distribution of the SN Ia to SN cc ratio in Abell 3112 out to R_{200} obtained from the fits of X-ray spectra with I99 WDD SN yields. The statistical errors corresponding to $\Delta C = 1$ with the systematic uncertainties described in Section 4 are added to the total error budget shown in the figure. The ratio of the SN Ia to SN cc is fairly uniform from the core to the outskirts.

with W7, CDD, and WDD models. A slight C-stat discrepancy between W7 and WDD (and CDD) models can be due to the underpredicted Si abundance in W7 models. However, due to the saddle difference in abundance yields of elements that are available to us in CCD resolution observations, we cannot distinguish between W7, W70, CDD, and WDD models in this work.

Additionally, we find that M10 CDDT model produces a significantly worse fit to the data (ΔC-stat $= 65$ for 840 dof) compared to the 1D deflagration and detonation SN Ia models. The current *Suzaku* CCD observations can already confirm that there is a disagreement between the *Suzaku* observations core region of Abell 3112 and the M10 CDDT model. The underlying reason is the overpredicted Si abundance and underpredicted Mg abundance in the M10 CDDT model compared to observations in the core region (Region 1). A similar tension in *XMM-Newton* observations of a large sample of clusters is reported by Mernier et al. (2016). The authors suggest that the observed discrepancy is due to a high Si/Fe ratio requested by the CDDT model, similarly to our conclusion. Lastly, we find a better agreement with the ODDT model and the *Suzaku* data, as compared to the M10 CCDT model. This agreement is also noted in Mernier et al. (2016).

We note that the goal of the paper is to determine the distribution of SN fraction out to R_{200} rather than individually testing the SN Ia models. Therefore we use the I99 WDD SN Ia and I99 SN cc yields providing the best-fit to the highest signal-to-noise data we have here in determining SN fractions. In the *snapec* model fits of Region 1, the model parameters N_{SNe}, R, kT, redshift, and normalization are left free. The best-fit parameters of the *snapec* models are given in Table 8. The temperature measurements between 2T *snapec* (5.29 ± 0.2 keV, 3.24 ± 0.12 keV) and 2T *apec* fits are consistent with each other within the 1σ confidence level. The best-fit N_{SNe} and R are respectively $(3.24 \pm 0.10) \times 10^9$ and 0.12 ± 0.02. To calculate the total number of SN explosions that enrich the ICM, the parameter N_{SNe} should be rescaled with the projected gas mass within the spectral extraction region (see Bulbul et al. 2012b for details). The gas mass within $0'–2'$ is $3.3 \times 10^{12} M_\odot$ (see Bulbul et al. 2012a, for mass profiles). Applying a conversion factor of 3.3 (in the units of $10^{12} M_\odot$), we find that the ICM of the core of Abell 3112 has been enriched by a total of $1.00 \pm 0.03 \times 10^9$ SN explosions within a 12.5 billion year period. This result is consistent with the reported total number of SN explosions ($1.06 \pm 0.34 \times 10^9$) from *XMM-Newton* observations (Bulbul et al. 2012b).

The observed fraction R in the *Suzaku* observations corresponds to a SN Ia fraction of 11% in the $0'–2'$ region of the cluster. We note that in their results Bulbul et al. (2012b)
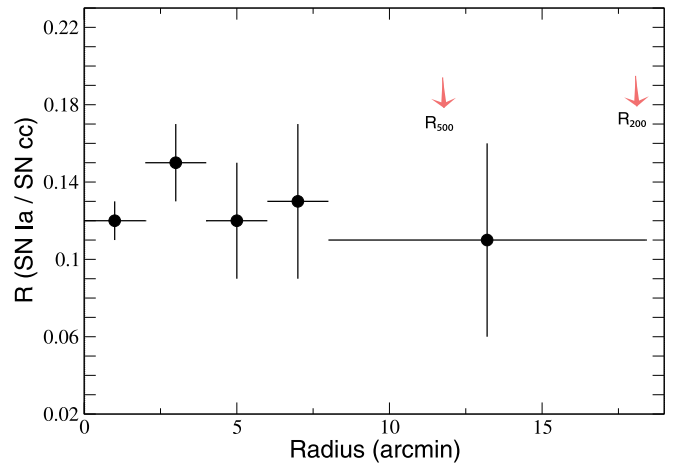
report a SN Ia fraction of $\sim$30% in the inner 52 kpc ($0'.6$) core region of the cluster. The discrepancy in the SN Ia fraction indicates that the SN fraction is diluted by the large PSF size of the *Suzaku* mirrors. The observed difference of the radial profiles of SN Ia products (e.g., S and Si between the *XMM-Newton* and *Suzaku* observations) indeed indicates a similar offset.

Using the I99 WDD models in the *snapec* fits of Region 2, we find that N_{SNe} is $1.96 \pm 0.36 \times 10^9$, while R is 0.16 ± 0.02 with C-stat $= 1079.9$ (for 842 dof). The reported enclosed gas mass is $7 \times 10^{12} M_\odot$ in Region 2, based on the Bulbul et al. (2010) models (see Bulbul et al. 2012b). Normalizing the N_{SNe} with a factor of 7, we find that the total number of SN explosions enriching the ICM in Region 2 is $(2.8 \pm 0.5) \times 10^8$ within 12.5 billion years.

The low signal-to-noise data in the spectra of Regions 3, 4, and 5 do not allow us to determine both N_{SNe} and normalization of the *snapec* model simultaneously, due to the degeneracy between these variables. The normalization of the *snapec* model is essentially determined from the continuum level, and it should be consistent with the normalization parameter of the *apec* model. We therefore use the normalization constrained from the *apec* model fits for the spectra of Regions 3, 4, and 5, and allow them to vary within their 1σ ranges. The best-fit parameters of the *snapec* model obtained with this method are shown in Table 8. For all the spectra we find acceptable fits to the *snapec* model.

The distribution of R (=SN Ia/SN cc) is shown in Figure 4 from the cluster core out to R_{200}. We note that the systematic uncertainties are included in the error bars shown in the figure. We find that the SN Ia and SN cc ratio, R, is consistent with a uniform SN Ia contribution to the enrichment, with $R \sim 0.13$. The SN Ia fraction of 12%–16% (of the total SN explosions) is consistent with the enrichment of the solar neighborhood (Tsujimoto et al. 1995). This uniformity suggests that both SN Ia and SN cc enrichment of the ICM outside of the core occurred at an early epoch. Since star formation in galaxy clusters occurs at $z > 2$ (Tran et al. 2007), this implies that the SN Ia that enrich the ICM are of the prompt variety, exploding with short delay following this early epoch of star formation. A similar conclusion is inferred from measurements in the low

redshift Perseus and Virgo clusters (Werner et al. 2013; Simionescu et al. 2015), and the early enrichment timescale is consistent with studies of mass-selected samples of galaxy clusters with redshift $0 < z < 1.5$ (Ettori et al. 2015; McDonald et al. 2016).

6. Conclusions

In this work we present an analysis of deep *Suzaku* (1.2 Ms of total XIS exposure) and *Chandra* (72ks) observations of Abell 3112, to constrain the distribution of SN enrichment of the ICM from the cluster core out to the cluster's virial radius using various published SN yields (Iwamoto et al. 1999; Nomoto et al. 2006; Maeda et al. 2010). To constrain the SN fraction, we use an *XSPEC* model, which is capable of fitting X-ray spectra with pre-defined SN yields from the literature.

Deep *Suzaku* observations of this relaxed archetypal cluster allow us to measure the plasma temperature and metal abundance out to the cluster's virial radius. We find that temperature constraints from *Suzaku* observations are in agreement with previous *XMM-Newton* observations within R_{500}. The temperature profile peaks around ~ 4.7 keV and declines to 3.12 ± 0.70 keV around the virial radius of the cluster.

We are also able to extend the measurements of metal abundances out to the cluster's virial radius. We find that the metallicity of the ICM is $0.22 \pm 0.08\, Z_{\odot}$ in the outskirts of the cluster near the virial radius and is consistent with the reported metallicities in nearby clusters (Werner et al. 2013; Simionescu et al. 2015; Bulbul et al. 2016b). The observed decline in the Fe abundance is steeper compared to the Mg profile; however, the Fe profile becomes uniform beyond the overdensity radius of $0.2 R_{200}$.

We find that the W7, CDD, and WDD SN Ia models produce similar goodness of the fit to the *Suzaku* data. The best-fit SN fraction and the total number of SN parameters obtained from these models are consistent with each other. However, a 2D delayed detonation SN Ia model M10 CDDT produces significantly worse fits to the X-ray spectrum of the central region of the cluster. This suggests that the CDDT models are insufficient to reproduce observed metal abundances (e.g., Si and Mg) in the cores of cluster of galaxies. Nonetheless, accurate testing of SN Ia models using galaxy cluster spectroscopy requires higher spectral resolution. Unfortunately, it will have to wait for the launch of the next calorimeter mission (see Bulbul et al. 2012b; Pointecouteau et al. 2013).

The distribution of the SN Ia fraction to the total number of SN explosions changes between 12% and 16% based on the I99 WDD delayed detonation models, which produce the best-fit to the X-ray spectra. This fraction is consistent with the observed fraction in our Galaxy and proto-solar abundances (15%–25%; Tsujimoto et al. 1995). We find that the distribution of the SN Ia fraction is fairly uniform out to the cluster's virial radius. The homogenous SN fraction points to an early ($z \sim 2$–3) metal enrichment and mixing, originating from an intense period of star formation activity in the cluster outskirts, and it also suggests that the metals are well-mixed into the ICM. Furthermore, our results are in agreement with the early enrichment timescale inferred from nearby Perseus and Virgo clusters (Werner et al. 2013; Simionescu et al. 2015) and a mass-selected sample of galaxy clusters reported by McDonald et al. (2016).

References

Anders, E., & Grevesse, N. 1989, GeCoA, 53, 197
Arnaud, K. A. 1996, adass V, 101, 17
Baldi, A., Ettori, S., Mazzotta, P., Tozzi, P., & Borgani, S. 2007, ApJ, 666, 835
Baumgartner, W. H., Loewenstein, M., Horner, D. J., & Mushotzky, R. F. 2005, ApJ, 620, 680
Bautz, M. W., Miller, E. D., Sanders, J. S., et al. 2009, PASJ, 61, 1117
Böhringer, H., Matsushita, K., Churazov, E., Finoguenov, A., & Ikebe, Y. 2004, A&A, 416, L21
Bonamente, M., Nevalainen, J., & Lieu, R. 2007, ApJ, 668, 796
Braglia, F. G., Ade, P. A. R., Bock, J. J., et al. 2011, MNRAS, 412, 1187
Bulbul, E., Markevitch, M., Foster, A., et al. 2016a, arXiv:1605.02034
Bulbul, E., Randall, S. W., Bayliss, M., et al. 2016b, ApJ, 818, 131
Bulbul, E., Smith, R., Foster, A., et al. 2012a, ApJ, 747, 32
Bulbul, E., Smith, R. K., & Loewenstein, M. 2012b, ApJ, 753, 54
Bulbul, G. E., Hasler, N., Bonamente, M., & Joy, M. 2010, ApJ, 720, 1038
Buote, D. A., Lewis, A. D., Brighenti, F., & Mathews, W. G. 2003, ApJ, 595, 151
De Grandi, S., Ettori, S., Longhetti, M., & Molendi, S. 2004, A&A, 419, 7
De Grandi, S., Santos, J. S., Nonino, M., et al. 2014, A&A, 567, A102
De Luca, A., & Molendi, S. 2004, A&A, 419, 837
de Plaa, J., Werner, N., Bleeker, J. A. M., et al. 2007, A&A, 465, 345
Dupke, R. A., & White., R. E., III 2000, ApJ, 528, 139
Ettori, S., Baldi, A., Balestra, I., et al. 2015, A&A, 578, A46
Finoguenov, A., David, L. P., & Ponman, T. J. 2000, ApJ, 544, 188
Foster, A. R., Ji, L., Smith, R. K., & Brickhouse, N. S. 2012, ApJ, 756, 128
Fujita, Y., Tawa, N., Hayashida, K., et al. 2008, PASJ, 60, S343
Hickox, R. C., & Markevitch, M. 2006, ApJ, 645, 95
Ishimaru, Y., & Arimoto, N. 1997, PASJ, 49, 1
Ishisaki, Y., Maeda, Y., Fujimoto, R., et al. 2007, PASJ, 59, 113
Iwamoto, K., Brachwitz, F., Nomoto, K., et al. 1999, ApJ, 125, 439
Kalberla, P. M. W., Burton, W. B., Hartmann, D., et al. 2005, A&A, 440, 775
Lehto, T., Nevalainen, J., Bonamente, M., Ota, N., & Kaastra, J. 2010, A&A, 524, A70
Lodders, K., & Palme, H. 2009, M&PSA, 72, 5154
Loewenstein, M. 2006, ApJ, 648, 230
Maeda, K., Röpke, F. K., Fink, M., et al. 2010, ApJ, 712, 624
Markevitch, M., Bautz, M. W., Biller, B., et al. 2003, ApJ, 583, 70
Matsushita, K., Böhringer, H., Takahashi, I., & Ikebe, Y. 2007, A&A, 462, 953
McDonald, M., Bulbul, E., de Haan, T., et al. 2016, ApJ, 826, 124
Mernier, F., de Plaa, J., Pinto, C., et al. 2016, arXiv:1608.03888
Moretti, A., Campana, S., Lazzati, D., & Tagliaferri, G. 2003, ApJ, 588, 696
Moretti, A., Pagani, C., Cusumano, G., et al. 2009, A&A, 493, 501
Mushotzky, R. F., & Loewenstein, M. 1997, ApJL, 481, L63
Nevalainen, J., Lieu, R., Bonamente, M., & Lumb, D. 2003, ApJ, 584, 716
Nomoto, K., Tominaga, N., Umeda, H., Kobayashi, C., & Maeda, K. 2006, NuPhA, 777, 424
O'Dea, C. P., Baum, S. A., Privon, G., et al. 2008, ApJ, 681, 1035
Pointecouteau, E., Reiprich, T. H., Adami, C., et al. 2013, arXiv:1306.2319
Portinari, L., Moretti, A., Chiosi, C., & Sommer-Larsen, J. 2004, ApJ, 604, 579
Simionescu, A., Werner, N., Böhringer, H., et al. 2009, A&A, 493, 409
Simionescu, A., Werner, N., Urban, O., et al. 2015, ApJL, 811, L25
Smith, R. K., Brickhouse, N. S., Liedahl, D. A., & Raymond, J. C. 2001, ApJL, 556, L91
Snowden, S. L., Mushotzky, R. F., Kuntz, K. D., & Davis, D. S. 2008, A&A, 478, 615
Takizawa, M., Sarazin, C. L., Blanton, E. L., & Taylor, G. B. 2003, ApJ, 595, 142
Tawa, N., Hayashida, K., Nagai, M., et al. 2008, PASJ, 60, 11
Tran, K. V. H., Franx, M., Illingworth, G. D., et al. 2007, ApJ, 661, 750
Tsujimoto, T., Nomoto, K., Yoshii, Y., et al. 1995, MNRAS, 277, 945
Werner, N., de Plaa, J., Bleeker, J. A. M., et al. 2006, A&A, 449, 475
Werner, N., Urban, O., Simionescu, A., & Allen, S. A. 2013, Natur, 502, 656